Flow characteristics and dispersion during the leakage of high pressure CO_2 from an industrial scale pipeline

Xiaolu Guo [a 1], Shaoyun Chen [b], Xingqing Yan [a], Xinyan Zhang [a], Jianliang Yu [a†], Yongchun Zhang [b], Haroun Mahgerefteh [c], Sergey Martynov [c], Alexander Collard [c], Solomon Brown [c 2]

[a] School of Chemical Machinery and Safety,
Dalian University of Technology, Dalian, 116024,China

[b] School of Chemical Engineering,
Dalian University of Technology, Dalian, 116024, China

[c] Department of Chemical Engineering,
University College London, London WC1E 7JE, UK

[†] Corresponding Author. Address
No 2 Ling Gong Road
Dalian, 116024, China
E-mail: yujianliang@dlut.edu.cn

Manuscript submitted to *International Journal of Greenhouse Gas Control*

September, 2017

[1] Current address: Hefei General Machinery Research Institute, Hefei, 230031, China. E-mail: xiaolu_guo@outlook.com

[2] Current address: Department of Chemical and Biological Engineering, University of Sheffield, Sheffield, London S1 3JD, UK

Flow characteristics and dispersion during the leakage of high pressure CO_2 from an industrial scale pipeline

Xiaolu Guo [a 1], Shaoyun Chen [b], Xingqing Yan [a], Xinyan Zhang [a], Jianliang Yu [a†], Yongchun Zhang [b], Haroun Mahgerefteh [c], Sergey Martynov [c], Alexander Collard [c], Solomon Brown [d 2]

Abstract

Pressurized pipelines represent a key way of transporting CO_2 from emitter to storage site. Leakage of CO_2 through a small puncture is the most common form of pipeline failure during normal operation; such failures could lead to fracture. The study of pipeline depressurization and dispersion behavior is of paramount importance for assessing the possibility of fracture propagation and the impact of CO_2 releases on the surrounding environment. A large-scale pipeline (258 m long, 233 mm i.d.) was constructed to study the flow characteristics and dispersion of gaseous, dense and supercritical phase CO_2 during vertical leakage through a 15 mm diameter orifice. The fluid pressures and temperatures in the pipeline were recorded to study the pressure response and phase transition inside the pipeline. Video cameras and CO_2 concentration sensors were used to monitor the formation of the visible cloud and the concentration distribution in the far-field. There was a "two cold, intermediate hot" phenomenon during the vertical leakage in the dense and supercritical release due to the dry ice particle accumulation near the orifice. The intersection of the jet flow and settling CO_2 mixture resulted in complex visible cloud forms in dense CO_2 release.

Keyword: CO_2 leakage, Flow characteristic, Dispersion, Large-scale pipeline.

1 Introduction

Carbon capture and storage (CCS) [1] represents a promising emissions mitigation method for achieving the objectives of decreasing greenhouse gas emissions while also allowing the continuation of fossil fuel use in order to meet already pressing energy demands. The technology involves capturing CO_2 from large industrial point sources of emission and then storing it in a reservoir instead of allowing its release to the atmosphere [2, 3].

CO_2 transportation is a key component of the CCS chain to transmit large amounts of CO_2 from emitter to storage site [4, 5]. Due to equipment failures, corrosions, maintenance errors, external impacts and operator errors the accidental leakages will inevitably occur in high pressure CO_2 pipelines [6]. The hazards associated with accidental releases from CO_2 pipelines include the toxic hazards of high CO_2 concentrations as well as of inventory impurities on humans and the environment [7]. A long running-ductile fracture may also be initiated by a puncture, such a possibility requires careful consideration when designing and operating CO_2 pipelines [8]. During the accidental rupture of a high pressure CO_2 pipeline a series of expansion waves will propagate from the rupture into the undisturbed fluid at the local speed of sound [9]. Significant Joule-Thomson cooling accompanying the initial expansion could lead to the formation of dry ice particles and the condensation water vapor in the jet flow, resulting in a visible cloud [10, 11]. Due to the relatively high density of gaseous CO_2 at ambient conditions the escaping CO_2 will rapidly concentrate in low-lying areas [12].

Many experimental studies have recently been performed to analyze depressurization behavior and dispersion during the release of CO_2 from pipelines. DNV-GL [13] used a 30 m long, 2 inch diameter spiral pipe to study fast depressurization of liquid CO_2 inventories to determine the level of low temperatures reached during this process. INERIS [14, 15] built a 2 m^3 spherical vessel to measure temperatures and gas concentrations in the dispersion region during CO_2 releases. An important observation from this work was that significant solids are generated within the near-field of dense phase releases, despite the inventory initially containing no dry ice itself. Witlox et al. [16, 17] reported release experiments conducted by BP and Shell during the CO_2 PIPETRANS JIP, including both high pressure cold CO_2 and supercritical hot CO_2 releases through nozzles. In these experiments solid CO_2 formed in the near-field and sublimed rapidly, no fallout was predicted for all cases. Xie et al. [18, 19] studied the vertical release of supercritical CO_2 from a 23 m long circulating pipe with a 30 mm inner diameter. A typical highly under-expanded jet flow structure was observed near the orifice. DNV-GL [20] developed a 0.5 m^3 pressurized vessel equipped with an actuator valve to discharge liquid CO_2. The measured CO_2 concentrations in the dispersion zone tended to increase continuously while saturated liquid was being discharged and then to drop with the transition to vapor outflow. The COSHER JIP [21] carried out a rupture test using a 3.3 m long pipe connected to a large-scale pipeline loop charged with circa 150 tons of CO_2 to study pipeline depressurization and dispersion of an initially dense phase inventory. Overall, most experimental research focused on horizontal releases from a small scale CO_2 pipeline using a valve control [22].

In the actual operation of a pipeline, a small puncture resulting in a leak oriented perpendicular to the long axis of the pipeline is the most probable form of failure. As part of the CO_2QUEST project [23-27], this paper presents the flow characteristics and dispersion of gaseous, dense and supercritical phase CO_2 (99.9 % pure) during vertical releases through a 15 mm diameter orifice in a 258 m long, 233 mm i.d. pipeline.

2 Experiments

2.1 Experimental setup

Fig. 1 shows a schematic of experimental apparatus. The experimental apparatus consisted of two CO_2 injecting lines, a 257 m long main pipeline built in 16MnD low temperature carbon steel, a 1 m long dual-disc blasting pipe and a 90° bend pipe built in grade 304 stainless steel, a heating system using 50 kW heating tape and a 50 mm thick thermal insulation layer. The pipeline was supported at a height of 1.3 m above ground with 24 concrete column foundations.

As shown in Fig. 2, the dual-disc blasting device consisted of two rupture discs and two disc holders, a solenoid valve, a 0.6 m long pipe (section I) and a 0.3 m long pipe (section II), it was designed to quickly and controllable open the pipeline and initiate experiments. To initiate the experiment, the pressure P_2 in section I was raised sharply, forcing the disc B to burst, disc A subsequently opened due to the decrease of the offset pressure. The 90° bend pipe used a long radius elbow to minimize pressure loss in the bend in order to better model vertical leakage from a small hole in an actual CO_2 pipeline. The bend pipe had a developed length of 0.85 m, an inner diameter of 50 mm and a wall thickness of 13 mm.

2.2 Instrumentation

Along the pipeline, 4 low frequency pressure sensors, 10 high frequency pressure sensors, 18 K-type thermocouples on the upper half of pipeline and 6 K-type thermocouples on the bottom half of pipeline were installed to monitor pressure and temperature changes inside the pipeline. The low frequency pressure sensors had a frequency response of 1 kHz and an accuracy of 0.25 % of full scale. The high frequency pressure sensors had a frequency response of 100 kHz and an accuracy of 0.25 % of full scale. The K-type thermocouples had a response time of 100 ms and uncertainty of ±1 °C. The orientations of these measurement points along the pipeline cross-section are shown in Fig. 3. Two high frequency pressure sensors (P_{s1} and P_{s2}) were mounted to measure the pressure loss inside the bend pipe. The locations of these measurement points are shown in Fig. 2.

20 CO_2 concentration sensors were arranged in the dispersion zone at a height of 1.3 m above ground. CO_2 concentration was measured using COZIR-W CO_2 concentration sensors, these have a response time of 4 s, a range of 0 to 100 % and an accuracy of ±3 %. Fig. 4 shows the measurement locations of these CO_2 concentration sensors in the dispersion zone. The x direction is parallel to the long axis of the pipeline and the y direction is horizontal distance (parallel with ground level).

The NI cRIO-9025 system was used to sample simultaneously 4 low frequency pressure sensors and all thermocouples. The NI cDAQ-9188 system was used to sample the 8 high frequency pressure sensors. The RS485 communication system was used to sample the CO_2 concentration sensors. A weather station was established to record ambient temperature, pressure, humidity, wind speed and direction. Several digital HD video cameras were used to record the evolutions of the visible clouds during experiments.

2.3 Experiments conducted

In this paper the flow characteristics and dispersion of pure gaseous, dense and supercritical phase CO_2 released vertically through a 15 mm diameter orifice are reported. The initial experimental conditions and environmental conditions of three tests are presented in Table 1. Through the environmental wind speeds were small, because the sky was overcast on the day the atmospheric stabilities were set as D. The instrument types, numbers and locations of the selected instruments are reported in Table 2.

3 Experimental results

3.1 Pressure developments during depressurization

Fig. 5, 6 and 7 show the evolutions of fluid pressures after rupture for tests 1, 2 and 3. The total depressurization times for the three experiments were 1620 s, 9200 s and 3300 s respectively. As shown in Fig. 5, 6 and 7, When the disc B burst, the pressures P_{s1} and P_{s2} rose sharply and then decreased exponentially with time, subsequently rose rapidly again due to the bursting of disc A. It was observed that the difference between the pressures inside the bent and the main pipelines was small after both discs were ruptured.

The rightward pointing arrow ("→") and the leftward pointing arrow ("←") indicate the direction of decompression wave propagation along the pipeline. The numbers above the arrows represent the times for the decompression wave to travel the length of the pipe and their propagation velocities in the 1st and 2nd periods. The pressure drop amplitude (ΔP_d), the pressure rebound amplitude (ΔP_r) and the quasi-static pressure (P_{qs}) of P_2 in the 1st period are presented in the magnified regions in Fig. 5, 6 and 7. Tables 3, 4 and 5 present the part values of pressure response parameters of P_2, P_6, P_7 and P_9 for test1, 2 and 3 respectively.

As shown in Fig. 5 and Table 3, in the 1st period after rupture the pressures of P_{s1} and P_{s2} rose to the first P_{qs} of 3.66 MPa and 3.61 MPa respectively due to the arrival of the expansion wave. For P_2, P_6, P_7 and P_9, the inventory pressures dropped successively when the decompression wave arrived and subsequently recovered to P_{qs1} due to droplet formation and gasification. ΔP_d and ΔP_r reduced greatly with the increase in distance of the measured point to the orifice. In the 2nd period the reflected decompression wave travelled from the closed end of the pipe to the orifice, causing a further decrease in pressures. For P_9, P_7 and P_6, the pressure achieved P_{qs2} and ΔP_d and ΔP_r reduced successively. As the decompression wave reflected repeatedly, ΔP_d, ΔP_r and P_{qs} reduced gradually until the pressure drop and rebound inside the pipeline disappeared. Whenever the decompression wave propagated to the orifice, the numbers of the P_{qs} of P_2, P_{s1} and P_{s2} would less one than those of P_6, P_7 and P_9. The pressure losses after the necking and the bend were very small in the 1st and 3rd periods, circa 0.02 MPa and 0.05 MPa, and 0.02 MPa and 0.06 MPa respectively.

As shown for test 2 in Fig. 6, during phase I of depressurization a sharp decline in pressure was observed, lasting about 30 s. During phase II the inventories achieved the saturation pressure (P_S), initially at a pressure of 5.46 MPa, lasting circa 6470 s. When inventory properties reached the triple point pressure (P_T) the phase III begins, this phase lasted about 2700 s. As shown in Table 4, the trends in pressure response parameters for test 2 were similar to those for test 1, but the values of ΔP_d, ΔP_r and P_{qs} for test 2 were larger than that for test 1 due to the lower compressibility of dense phase CO_2. In the 1st period of the dense tests there was an obvious slowdown between sharp decline and rapid rise in pressures compared to those seen in test 1 as a result of bubble nucleation in the superheated state. The pressure losses after the necking and the bend in the 1st and 3rd period were circa 0.09 MPa and 0.11 MPa,and 0.08 MPa and 0.06 MPa respectively.

As shown in Fig. 7, during phase I of test 3, the pressure drop process was composed of about 20 passes and reflections of the decompression wave by circa 25 s. During phase II, the pressure of CO_2 dropped with the unique waveform by circa 135 s. In phase III, the pressure dropped slowly to ambient with no pressure fluctuations. As shown in Table 5, by comparing the depressurizations for tests 1, 2 and 3, the trends in pressure response parameters of the three tests were similar. Because the compressibility of supercritical CO_2 was close to that of gaseous CO_2 the values of ΔP_d, ΔP_r and P_{qs} for test 3 were slightly larger than those for test 1 and smaller than those for test 2. During the 1st period of test 3 there was a nonlinear sudden drop and a rapid rise in pressures as a result of bubble nucleation in the superheated state. It could be observed that the rate of pressure drop at P_2 stagnated when the pressure of CO_2 passed through P_c due to bubble nucleation. The pressure losses after the necking and the bend in the 1st and 3rd periods were circa 0.07 MPa and 0.11 MPa, and 0.04 MPa and 0.14 MPa respectively. It could be concluded that the pressure losses after the necking and the bend in the dense and supercritical CO_2 releases were slightly larger than those in the gaseous CO_2 release.

3.2 Phase transitions inside the pipeline

Fig. 8(a), (b) and (c) show the evolutions of the fluid pressure and temperature plotted on the CO_2 phase diagram for tests 1, 2 and 3. A is the initial phase in the figure, the points B and C are the locations of the various phase changes in these tests. Upon rupture, the instantaneous pressure drop was accompanied by a sharp temperature drop which caused phase changes in each test. As phase change was instantaneous after rupture it was not captured by the slow-response thermocouples. As shown in Fig. 8(a), because of the failures of the heating tape at T_2-P_2 and the slower rate of heat exchange in gaseous CO_2, the initial temperature of T_2-P_2 was lower than that at other points. As indicated by the recorded thermodynamic trajectories of test 1, no phase change was observed in the overall release process but the instantaneous phase transitions appeared at the beginning of the release. As shown in Fig. 8(b), after the start of release the inventory inside the pipeline rapidly achieved a saturation state (5.46 MPa) from point A to B, which corresponded to phase I of pipeline depressurization. During phase II of depressurization the saturation properties evolved from points B to E. T_{16}-P_{11}, T_7-P_5, T_2-P_2 and T_{16d}-P_{11} started successively to deviate from the saturation line at the point C, and T_{18}-P_{12} started to deviate from the saturation line at the point D. This result showed that the transition from gas-liquid phase CO_2 to gaseous CO_2 during depressurization occurred first at T_{16}-P_{11}, and then spread to the orifice along the top of pipe and to the closed end of pipe along the top of pipe. T_{18d}-P_{12} and T_{7d}-P_5 started successively to deviate from the saturation line at the point E (CO_2 triple point), and T_{2d}-P_2 didn't deviate from the saturation line until the end of the release. This result demonstrated the subsequent generation of dry ice particles at the bottom of the pipeline, changing the inventory mixture to gas-solid flow or gas-liquid-solid flow. Significant changes had taken place in the flow density due to the formation of dry ice particles which caused the pressure-temperature curves to fluctuate violently. As shown in Fig. 8(c), the supercritical CO_2 started to transform into the gas-liquid phase when the pressure dropped to P_c. T_{16}-P_{11}, T_7-P_5, T_2-P_2 and T_{16d}-P_{11} started successively to deviate from the saturation line at the point B, T_{18}-P_{12} at the point C, T_{18d}-P_{12} and T_{7d}-P_5 at the point D, and T_{2d}-P_2 at the point E. This result showed that the transition from gas-liquid to gaseous CO_2 occurred first at T_{16}-P_{11} and then spread to the orifice and the closed end of the pipe along the top surface first, then along the bottom of pipe. Because the change of the release direction during the vertical leakage made the secondary flow appeared inside the bend pipeline, a large amount of dry ice particles were accumulated and the temperature was lowest near the orifice, this phenomenon was different to the results from the horizontal release experiments [24, 25].

Fig. 9(a), (b) and (c) show the fluid temperature changes with time in the tests 1, 2 and 3. After rupture, the instantaneous pressure drops were accompanied by sharp temperature falls in each test, this change was not captured by the slow-response thermocouples. For test 1, because of the differences in initial temperatures between T_2, T_7, T_{2d}, T_{7d} and the slow heat exchange in gaseous CO_2, temperature stratification was observed inside the main pipe. After rupture, the temperatures at T_{2d} and T_{7d} dropped suddenly due to the pressure drop, then rose to 35.3 °C and 26.3 °C respectively as a result of the higher temperature from the upper stream. Eventually all inventory temperatures reached minimum values at 240 s and the maximum temperature drop amplitudes of T_2, T_7, T_{16}, T_{18}, T_{16d} and T_{18d} were 3.4 °C, 6.3 °C, 10.6 °C, 12.8 °C, 11.2 °C and 13.3 °C respectively. This suggested that the decreasing amplitude became larger with increasing distance from the orifice. Fluid temperatures recorded at the bottom of the pipe were slightly lower than those at corresponding distances at the top of the pipe in the gas phase test.

For test 2, in phase I all inventory temperatures dropped quickly from the initial temperature to the saturation temperature (18.0 °C). In phase II the temperatures at T_2, T_7 and T_{16} decreased to -33.5 °C, -33.0 °C, -27.0 °C, the temperature at T_{18} decreased to -40.5 °C before recovering to -36.0 °C, and the temperatures at T_{2d}, T_{7d}, T_{16d}, T_{18d} decreased to -55.2 °C, -54.2 °C, -29.7 °C and -52.1 °C respectively. This result showed that the largest temperature difference occurred at the bottom of the pipe near the release end and the smallest temperature difference appeared near the top of the pipe at T_{16}. In phase III the temperature inside the pipe fluctuated sharply due to the formation of dry ice particles. The lowest temperature reached was -74.3 °C at T_{2d} at the end of the release.

For test 3, the lowest temperatures observed at T_2, T_7, T_{16} were -5.6 °C, 0.9 °C and 10.6 °C. The temperature at Tf18 decreased to 1.2 °C before recovering to 7.8 °C, and at T_{2d}, T_{7d}, T_{16d} and T_{18d} the temperatures decreased to -34.9 °C, 0 °C, -2.0 °C and -16.7 °C before increasing to -19.0 °C,5.9 °C, 17.63 °C and 5.9 °C. This result demonstrated that the fluid temperature at the bottom of the pipe was lower than at the corresponding location at the top of the pipe, and that the lowest temperature occurred at the bottom of the pipe near the orifice. There was a "two cold, intermediate hot" phenomenon during the vertical release in the supercritical phase test due to dry ice particle accumulation near the orifice, it was similar to the results of the dense phase test.

3.3 Visible cloud dispersion and CO_2 concentration

According to the observations of the visible cloud, in test 1 the diffusion ranges were very small and the photographs of the cloud were of poor quality, thus no further discussion of test 1 was presented. Fig. 10 shows the development of the visible cloud for test 2. The diffusion process could be divided into rapid expansion (I), sedimentation (II) and slow attenuation stages (III). For test 2 the duration times of three stages were 20 s, 180 s and 9000 s respectively. In stage I, the sharp drop in inventory pressure near the orifice produced a highly under-expanded jet and induced a sharp drop in temperature as a result of Joule-Thomson cooling. This effect led to the formation of solid CO_2 particles inside the under-expanded jet and the condensation of water vapour at the jet boundary, this was subsequently entrained. In the far field the water vapour continued to condense from the ambient air as a result of jet expansion and CO_2 sublimation. The visible white cloud entraining the solid CO_2 particles and condensed water rapidly expanded in stage I, reaching a maximum height and width of 40 m and 12 m respectively. In stage II, due to the heavy gas effect of the cooled CO_2 and condensed water a clearly visible cloud settlement process could be observed in Fig. 10. The intersection of the jet flow and settling CO_2 cloud resulted in complex cloud forms. The ground wind speed was nil on the day, however the visible cloud deviated to one side at 180 s as a result of the intermittent wind at greater height. In stage III, the obvious settlement process had not been observed. The size of the visible cloud began to decrease and the attenuation velocity also decreased.

Fig. 11 shows the development of the visible cloud for test 3. The diffusion process could be divided into rapid expansion (I), metastable (II) and slow attenuation stages (III). For test 3 the duration times of the three stages were 2 s, 150 s and 3150 s respectively. In stage I, the distribution range of the visible cloud developed quickly to reach its maximum extent. Because the supercritical CO_2 had a lower viscosity and a higher flow velocity compared to the dense CO_2, the duration time for test 3 was shorter than for test 2. In stage II, the dimensions of the visible cloud remained largely unchanged. Due to faster diffusion and the lesser amount of supercritical CO_2 released compared to test 2, no significant settlement process was observed. The maximum dimensions of the visible cloud for test 3 were smaller than for test 2, circa 18 m and 3 m respectively. In stage III, the size of the visible cloud began to decay and the attenuation velocity decreased.

Fig. 12 shows the evolutions of CO_2 concentrations at 1.3 m above the ground for test 2. According to the observations of CO_2 concentration in tests 1 and 3, CO_2 concentrations at this height were always lower than 0.2 % due to the fast diffusion velocities of CO_2 in these tests. As shown in Fig. 12, the maximum CO_2 concentration at C(9 m, 1 m) was circa 5.1 %. The maximum CO_2 concentrations at C(7 m, 1 m), C(9 m, 1 m), C(11 m, 1 m), C(14 m, 1 m), C(7 m, 0 m), C(9 m, 2 m) were all above 3 %. This demonstrated that a large amount of CO_2 settled in the area around 9 m from the rupture. During settlement of the visible cloud in stage (II), the measured CO_2 concentrations were always above 3 %. From 180 s to 1000 s after rupture the measured CO_2 concentrations remained between 1 % and 3 %. After 1000 s the measured CO_2 concentrations fell below 1 %. Compared to the gaseous and supercritical CO_2 releases, in test 2 the escaping CO_2 more easily formed a relatively high concentration cloud at ground level.

3.4 Physical analyses

Based on the experimental observations and analysis presented above, the mechanisms of cloud flow characteristics and dispersion, common in the gaseous, dense and supercritical CO_2 experiments, are shown in Fig. 13. Following rupture the rapid expansion of the high pressure CO_2 at the orifice resulted in a decompression wave which propagated back and forth inside the pipeline. Passage of the decompression wave through the inventory caused the pressure undershoot and rebound to a quasi-static level successively. Compared to the results from the horizontal release experiments [24, 25], the release direction had no significant effect on the pressure response process. For the gaseous CO_2 test no phase change was observed in the overall release process (see fig 9a). For the dense CO_2 test, as the pressure declined the inventory transformed rapidly into a gas-liquid mixture and subsequently evolved to gas-solid or gas-liquid-solid phases as the pressure fell below P_T. For the supercritical CO_2 test, the inventory successively transformed into a gas-liquid mixture and then a pure gas phase fluid once the inventory pressure fell below P_c. In the supercritical and dense CO_2 test the solid fraction at the bottom of pipeline was larger than that at the top, but the gas phase fraction distribution was just the opposite. A “two cold, intermediate hot” phenomenon was observed during the vertical leakage in the dense and supercritical release. This was caused by the dry ice particle accumulation due to the circulation of fluid near the orifice. In the near-field dispersion zone the gas-solid two-phase flow observed in test 2 entrained a mass of dry ice particles, gaseous CO_2, air and condensed water, while continuing to spread in the far-field [26, 27]. The intersection of the jet flow and settling CO_2 mixture resulted in complex visible cloud forms.

The modeling of CO_2 pipeline rupture is commonly divided into two parts, the modeling of CO_2 flow characteristics inside the pipe and the modeling of CO_2 dispersion [28, 29]. Due to the rather complicated phenomena ocurring in the pipeline rupture process and the very high computational times of transient CFD simulations, it's very difficult to establish mathematical models for predicting such complicated releases from a high pressure CO_2 pipeline [30-32]. The large-scale experimental results reported are extremely valuable to the future development of a rigorous multiphase CO_2 outflow and dispersion model for predicting CO_2 flow characteristics and dispersion behavior following pipeline failure.

4 Conclusions

This article has presented large-scale experimental research of the flow characteristics inside a pipeline and the dispersion behaviour of gaseous, dense and supercritical phase CO_2 from a vertically oriented 15 mm diameter rupture. According to the experimental study, some conclusions are demonstrated as follows:

(1) When a small diameter rupture occurred, a decompression wave propagated back and forth along the pipeline. Passage of the decompression wave through the inventory caused pressure undershoot and rebound to a quasi-static level. For three phase CO_2 leakage, the change processes of the pressure responses and the pressure response parameters were different. Compared to the results from the horizontal release experiments [24, 25], the release direction had no significant effect on the pressure response process.

(2) For the dense and supercritical CO_2 test, with the pressure in continuous decline the initial phase was transformed rapidly into a gas-liquid mixture and subsequently a gas-solid or gas-liquid-solid mixture when the pressure fell below P_T. The solid fraction at the bottom of pipeline was larger than that at the top, but the gas phase fraction distribution was just the opposite. A "two cold, intermediate hot"

phenomenon was observed during the vertical leakage in the dense and supercritical release. This was caused by the dry ice particle accumulation due to the circulation of fluid near the orifice.

(3) For three phase CO_2 leakage, the gas-solid two-phase jet entrained a mass of dry ice particles, gaseous CO_2, air and condensed water in the near-field, this mixture continued to spread in the far-field. For the dense CO_2 release the escaping CO_2 more easily formed a relatively high concentration cloud at ground level, and a clearly visible cloud settlement process could be observed. The intersection of the jet flow and settling CO_2 mixture resulted in complex visible cloud forms in dense CO_2 release.

Acknowledgement

The authors would like to acknowledge the funding received from the European Union Seventh Framework Programmes FP7-ENERGY-2009-1 under grant agreement number 241346 and FP7-ENERGY-2012-1STAGE under Grant agreement 309102.

References

[1] Putman WM, Ott L, Darmenov A, DaSilva A. A global perspective of atmospheric carbon dioxide concentrations. Parallel Computing 2016; 55:2-8.

[2] Viebahn P, Vallentin D, Höller S. Prospects of carbon capture and storage (CCS) in China's power sector An integrated assessment. Appl Energy 2015; 157:229-244.

[3] IEA, Energy Technology Perspectives 2008, Paris: France, 2008.

[4] Lin CW, Nazeri M, Bhattacharji A, Spicer G, Maroto-Valer MM. Apparatus and method for calibrating a Coriolis mass flow meter for carbon dioxide at pressure and temperature conditions represented to CCS pipeline operations. Appl Energy 2016; 165:759-764.

[5] Molag M, Dam C. Modelling of accidental from a high pressure CO_2 pipelines . Energy Procedia. 2011; 4:2301-2307.

[6] Cosham A. The saturation pressure and the design of dense-phase CO_2 pipelines. J Pipeline Eng 2012; 3:213–230.

[7] Koornneef J, Ramírez A, Turkenburg W, Faaij A. The environmental impact and risk assessment of CO_2 capture, transport and storage – an evaluation of the knowledge base. Prog Energy Combust Sci 2012; 38: 62–86.

[8] Aursand E, Dumoulin S, Hammer M, Lange HL, Morin A, Munkejord ST, Nordhagen HO. Fracture propagation control in CO_2 pipelines: Validation of a coupled fluid–structure model. Engineering Structures 2016; 123:192–212.

[9] Woolley RM, Fairweather M, Wareing CJ, Prous J, Hebrard J, Jamois D, Narasimhamurthy VD, Storvik IE, Sælen L, Skjold T, Falle SAEG, Brown S, Mahgerefteh H, Martynov S, Gant SE, Tsangaris DM, Economou IG, Boulougouris GC, Diamantonis NI, An integrated, multi-scale modelling

approach for the simulation of multiphase dispersion from accidental CO_2 pipeline releases in realistic terrain. Int J Greenh Gas Con 2014; 27:221-238.

[10] Mazzoldi A, Hill T, Colls JJ. CO_2 transportation for carbon capture and storage: Sublimation of carbon dioxide from a dry ice bank. Int J Greenh Gas Con 2008 2:210-218.

[11] Harper P, Wilday J, Bilio M. Assessment of the major hazard potential of carbon dioxide (CO_2). Health and Safety Executive 2011; 1-28.

[12] Brown S, Martynov S, Mahgerefteh H, Proust C. A homogeneous relaxation flow model for the full bore rupture of dense phase CO_2 pipelines. Int J Greenh Gas Con 2013; 17:349-356.

[13] Vree B, Ahmad M, Buit L, Florisson O. Rapid depressurization of a CO_2 pipeline – an experimental study. Int J Greenh Gas Con 2015; 41:41–49

[14] Woolley RM, Fairweather M, Wareing CJ, Falle SAEG, Proust C, Hebrard J, Jamios D. Experimental measurement and Reynolds-averaged Navier–Stokes modelling of the near-field structure of multi-phase CO_2 jet releases. Int J Greenh Gas Con 2013; 18:139–149.

[15] Gant SE, Narasimhamurthy VD, Skjold T, Jamois D, Proust C. Evaluation of multi-phase atmospheric dispersion models for application to carbon capture and storage. J Loss Prevent Proc 2014; 32:286-298.

[16] Witlox HWM, Harper M, Oke A, Stene J. Phast validation of discharge and atmospheric dispersion for pressurised carbon dioxide releases. J Loss Prevent Proc 2014; 30:243-255.

[17] Witlox HWM, Harper M, Oke A, Stene J. Validation of discharge and atmospheric dispersion for unpressurised and pressurised carbon dioxide releases. Process Saf Environ 2014; 92:3-16.

[18] Xie QY, Tu R, Jiang X, Li K, Zhou XJ. The leakage behavior of supercritical CO_2 flow in an experimental pipeline system. Appl Energ 2014; 130:574-580.

[19] Li K, Zhou XJ, Tu R, Xie QY, Jiang X. The flow and heat transfer characteristics of supercritical CO_2 leakage from a pipeline. Energy 2014; 71:665-672.

[20] Ahmad M, Osch MB, Buit L, Florisson O, Hulsbosch-Dam C, Spruijt M, Dacolio F. Study of the thermohydraulics of CO_2 discharge from a high pressure reservoir. Int J Greenh Gas Con 2013; 19:63-73.

[21] Ahmad M, Lowesmith B, Koeijer Gd, Nilsen S, Tonda H, Spinelli C, Cooper R, Clausen S, Mendes R, Florisson O. COSHER joint industry project: Large scale pipeline rupture tests to study CO_2 release and dispersion. Int J Greenh Gas Con 2015; 37:340–353.

[22] Pham LHHP, Rusli R. A review of experimental and modelling methods for accidental release behaviour of high-pressurised CO_2 pipelines at atmospheric environment. Process Saf Environ 2016; 104:48–84.

[23] Brown S, Martynov S, Mahgerefteh H, Fairweather M, Woolley RM, Wareing CJ, Falle SAEG, Rutters H, Niemi A, Zhang YC, Chen SY, Besnebat J, Shah N, Dowell NM, Proust C, Farret R, Economou IG, Tsangaris DT, Boulougouris GC, Wittenberghe JV. CO_2QUEST: Techno-economic assessment of CO_2 quality effect on its storage and transport. Energy Procedia 2014; 63:2622-2629.

[24] Guo XL, Yan XQ, Yu JL, Zhang YC, Chen SY, Mahgerefteh H, Martynov S, Collard A, Proust C. Pressure response and phase transition in supercritical CO_2 releases from a large-scale pipeline. Appl Energ 2016; 178:189-197.

[25] Guo XL, Yan XQ, Yu JL, Yang Y, Zhang YC, Chen SY, Mahgerefteh H, Martynov S, Collard A. Pressure responses and phase transitions during the release of high pressure CO_2 from a large-scale pipeline. Energy 2016; 1-13.

[26] Guo XL, Yan XQ, Yu JL, Zhang YC, Chen SY, Mahgerefteh H, Martynov S, Collard A, Proust C. Under-expanded jets and dispersion in supercritical CO2 releases from a large-scale pipeline. Appl Energ 2016; 183:1279-1291.

[27] Guo XL, Yan XQ, Zheng YG, Yu JL, Zhang YC, Chen SY, Chen L, Mahgerefteh H, Martynov S, Collard A, Brown S. Under-expanded jets and dispersion in high pressure CO_2 releases from an industrial scale pipeline. Energy 2016; 119:53-66.

[28] Liu X, Godbole A, Lu C, Michal G, Venton P. Source strength and dispersion of CO_2 releases from high-pressure pipelines: CFD model using real gas equation of state. Appl Energ 2014; 126: 56-68.

[29] Xing J, Liu ZY, Huang P, Feng CG, Zhou Y, Zhang DP, Wang F. Experimental and numerical study of the dispersion of carbon dioxide plume. J Hazard Mater, 2013, 256-257:40-48.

[30] Mahgerefteh H, Atti O. Modeling low-temperature-induced failure of pressurized pipelines. AIChE J 2006; 52(3): 1248-1257.

[31] Mahgerefteh H, Atti O, Denton G. An interpolation technique for rapid CFD simulation of turbulent two-phase flows. Process Saf Environ 2007; 85(B1): 45-50.

[32] Wareing CJ, Fairweather M, Falle SAEG, Woolley RM. Modelling punctures of buried high-pressure dense phase CO_2 pipelines in CCS applications. Int J Greenh Gas Con 2014; 29:231-247.

Table s

Table 1 Experimental conditions and environmental conditions.

Number	Test1	Test2	Test3
Pressure (MPa)	3.7	9.0	8.4
Temperature (^{o}C)	37.5	19.9	35.7
Orifice (mm)	15	15	15
Inventory (tons)	0.85	9.2	6.1
Environmental pressure (kPa)	100.20	100.96	101.34
Environmental temperature (^{o}C)	13.5	16.2	16.0
Humidity (%)	87.8	91.4	73
Wind speed (m/s)	1.0	0	1.2
Wind direction	138	-	339
Atmospheric stability	D	D	D

Table 2 Experimental measurement point locations.

Temperature on top of the pipe	Temperature on bottom of the pipe	Pressure	Distance from the orifice (m)
T_2	T_{2d}		7.4
		P_2	10.4
T_4	T_{4d}	P_3	13.5
		P_4	22.3
T_7	T_{7d}	P_5	54.2
T_9	T_{9d}	P_6	62.1
		P_7	108.8
		P_8	116.8
		P_9	162.0
T_{16}	T_{16d}	P_{11}	237.4
T_{18}	T_{18d}	P_{12}	248.6

Table 3 Pressure response parameters of test 1.

Parameter (MPa)	P_2	P_6	P_7	P_9	Trend
1st pressure drop amplitude ΔP_{d1}	1.17	0.47	0.33	0.28	Decrease
1st pressure rebound amplitude ΔP_{r1}	1.15	0.45	0.31	0.26	Decrease
1st quasi-static pressure P_{qs1}	3.68	3.68	3.68	3.68	Similar
2nd pressure drop amplitude ΔP_{d2}	<u>0.15</u>	0.11	0.13	0.14	Increase
2nd pressure rebound amplitude ΔP_{r2}	<u>0.08</u>	0.10	0.12	0.13	Increase
2nd quasi-static pressure P_{qs2}	<u>3.61</u>	3.67	3.67	3.67	Similar
3rd pressure drop amplitude ΔP_{d3}	<u>0.08</u>	0.11	0.10	0.08	Decrease
3rd pressure rebound amplitude ΔP_{r3}	<u>0.13</u>	0.10	0.09	0.07	Decrease
3rd quasi-static pressure P_{qs3}	3.66	3.66	3.66	3.66	Similar

Table 4 Pressure response parameters of test 2.

Parameter (MPa)	P_2	P_6	P_7	P_9	Trend
1st pressure drop amplitude ΔP_{d1}	4.27	3.79	3.67	3.44	Decrease
1st pressure rebound amplitude ΔP_{r1}	4.07	3.59	3.47	3.24	Decrease
1st quasi-static pressure P_{qs1}	8.80	8.80	8.80	8.80	Similar
2nd pressure drop amplitude ΔP_{d2}	3.38	2.37	2.43	2.52	Increase
2nd pressure rebound amplitude ΔP_{r2}	3.09	2.33	2.39	2.38	Increase
2nd quasi-static pressure P_{qs2}	7.18	8.66	8.66	8.66	Similar
3rd pressure drop amplitude ΔP_{d3}	1.38	2.68	2.66	2.42	Decrease
3rd pressure rebound amplitude ΔP_{r3}	2.71	2.53	2.51	2.27	Decrease
3rd quasi-static pressure P_{qs3}	8.51	8.51	8.51	8.51	Similar

Table 5 Pressure response parameters of test 3.

Parameter (MPa)	P_2	P_6	P_7	P_9	Trend
1st pressure drop amplitude ΔP_{d1}	1.75	0.89	0.76	0.63	Decrease
1st pressure rebound amplitude ΔP_{r1}	1.70	0.84	0.71	0.58	Decrease
1st quasi-static pressure P_{qs1}	8.35	8.35	8.35	8.35	Similar
2nd pressure drop amplitude ΔP_{d2}	0.55	0.35	0.40	0.43	Increase
2nd pressure rebound amplitude ΔP_{r2}	0.25	0.31	0.36	0.39	Increase
2nd quasi-static pressure P_{qs2}	8.05	8.31	8.31	8.31	Similar
3rd pressure drop amplitude ΔP_{d3}	0.08	0.30	0.29	0.25	Decrease
3rd pressure rebound amplitude ΔP_{r3}	0.32	0.28	0.27	0.23	Decrease
3rd quasi-static pressure P_{qs3}	8.29	8.29	8.29	8.29	Similar

Figures

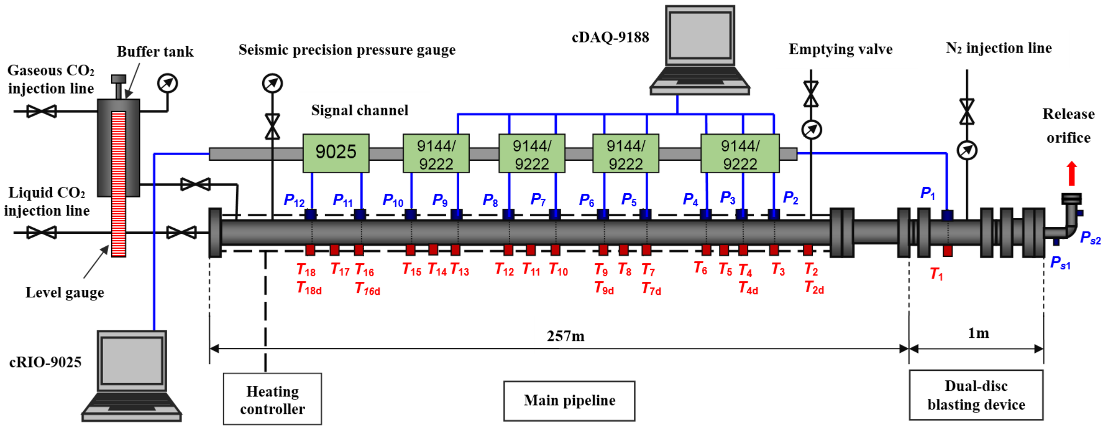

Fig. 1 Schematic and scene graph of experimental apparatus.

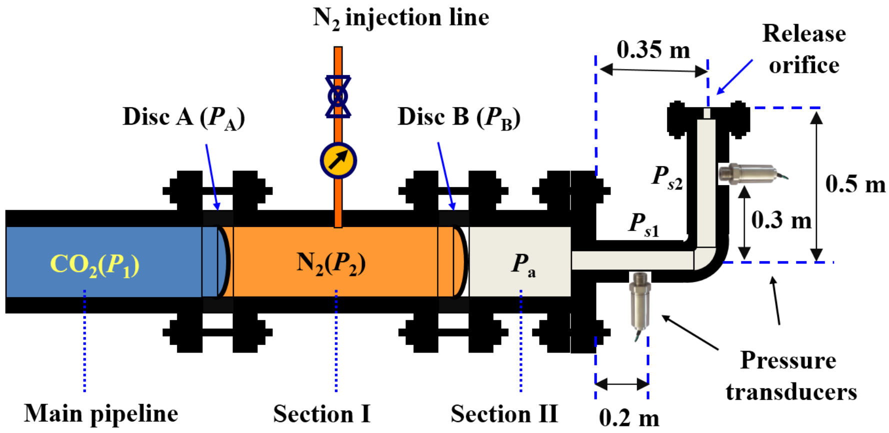

Fig. 2 Schematic of dual-disc blasting device and bend pipe.

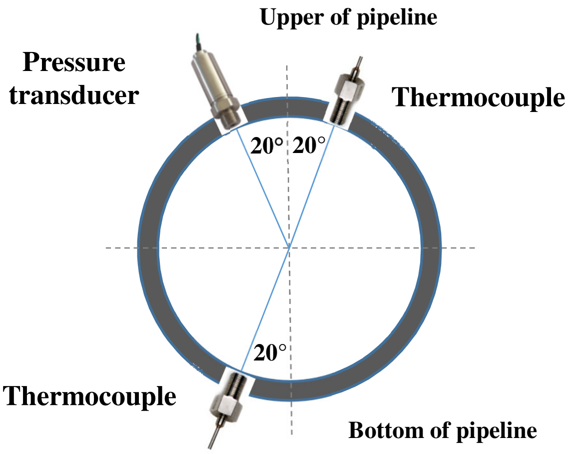

Fig. 3 Measurement point locations.

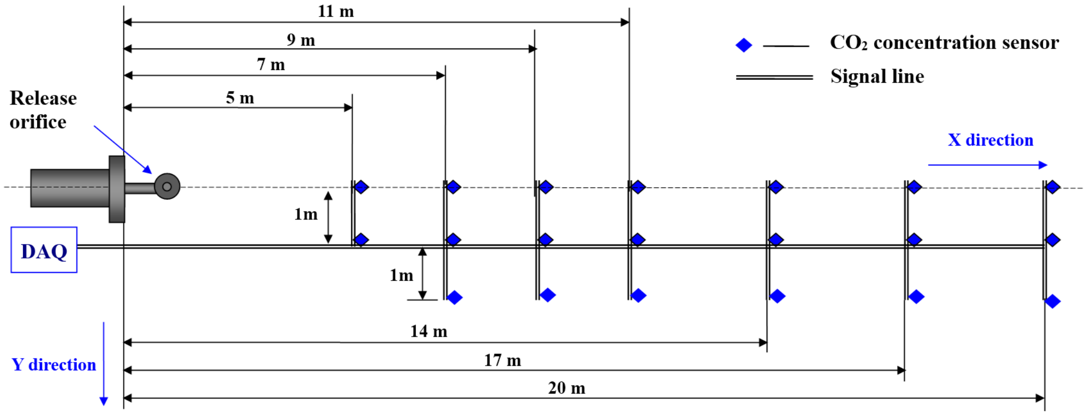

Fig. 4 Distribution of measurement points in discharge area.

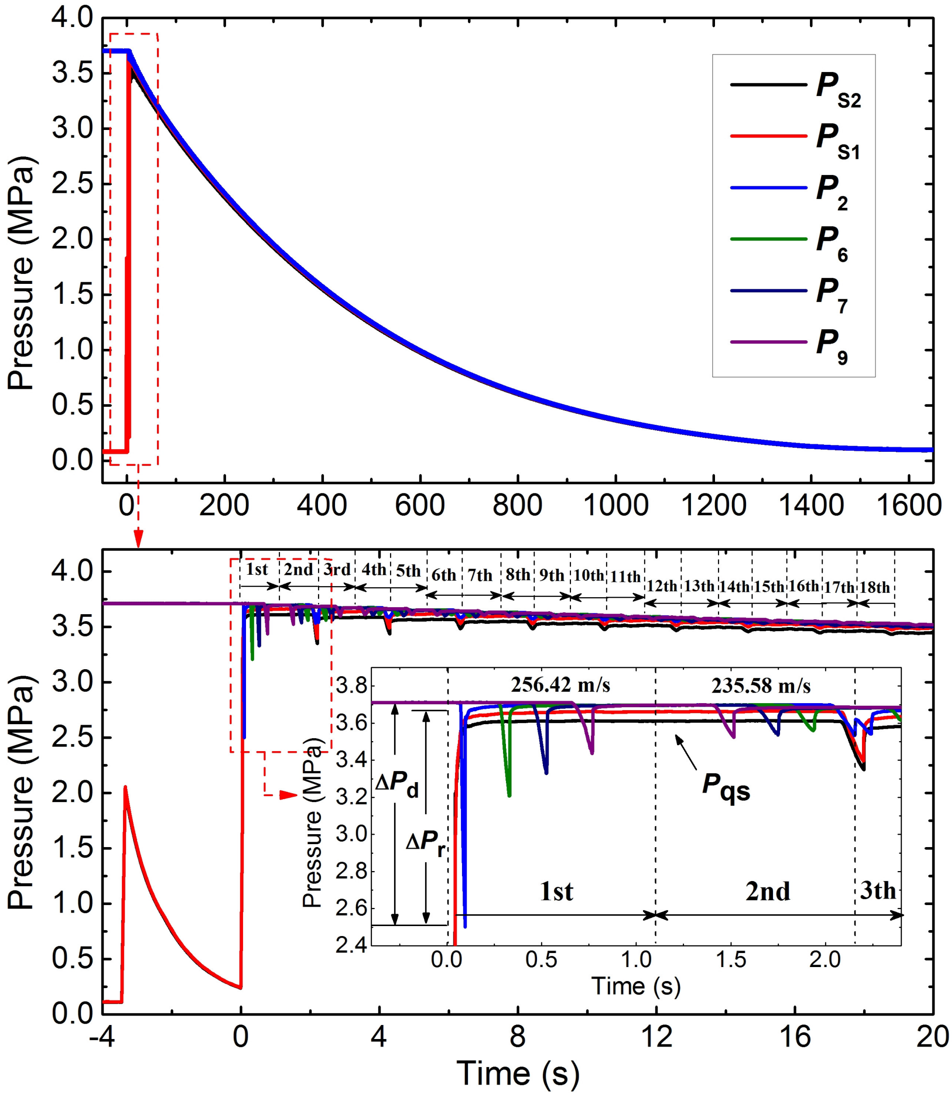

Fig. 5 Pressure evolutions of the gaseous CO_2 release experiment.

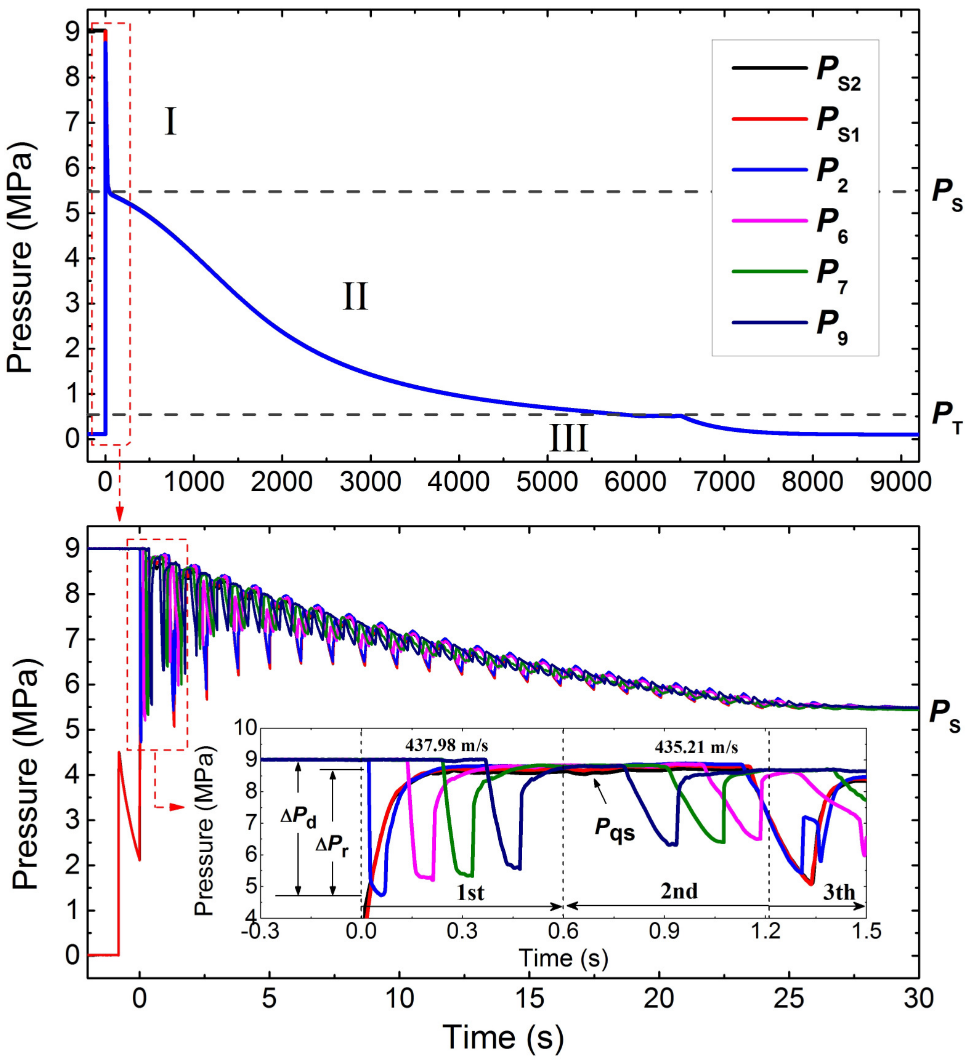

Fig. 6 Pressure evolutions of the dense CO_2 release experiment.

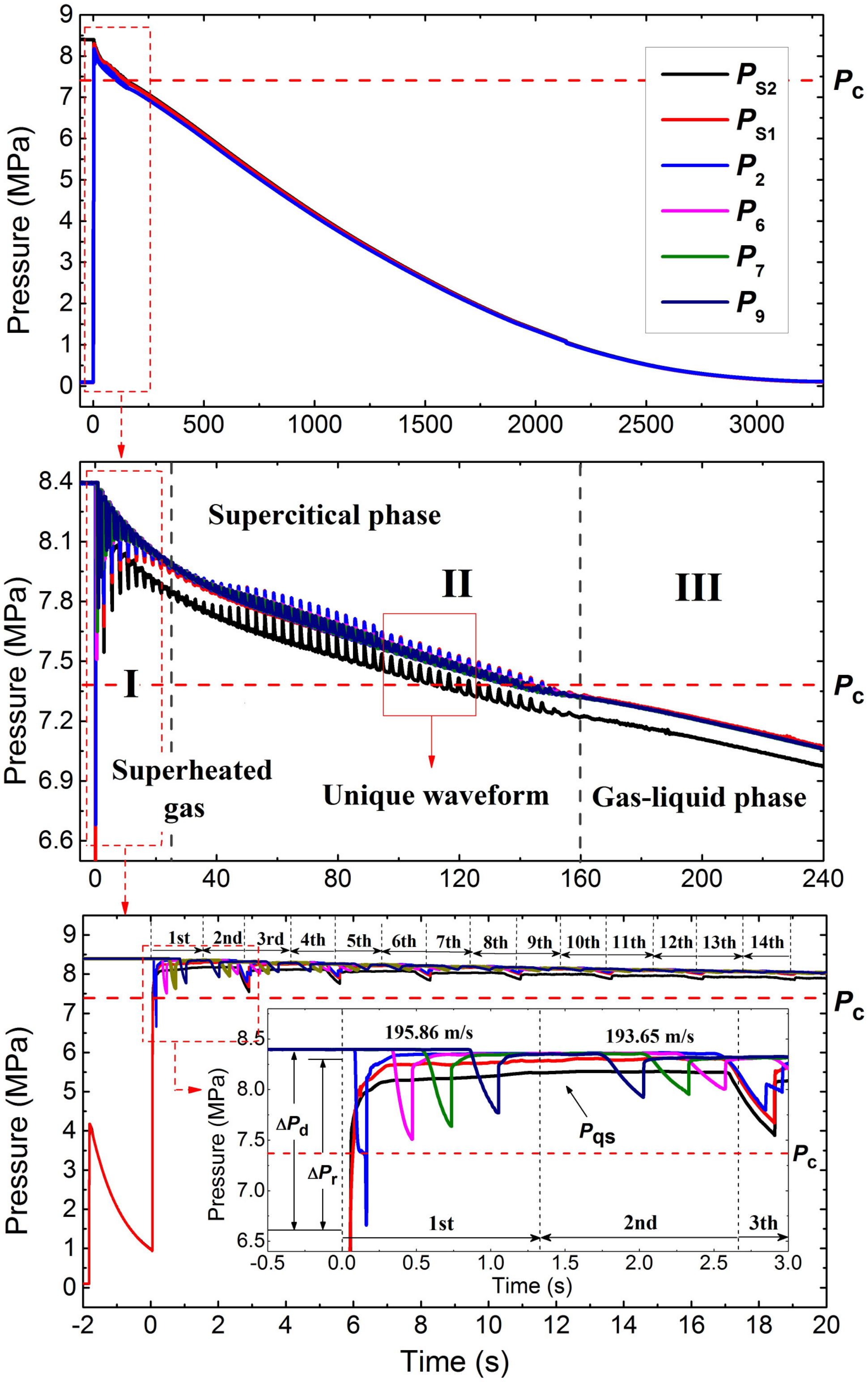

Fig. 7 Pressure evolutions of the supercritical CO_2 release experiment.

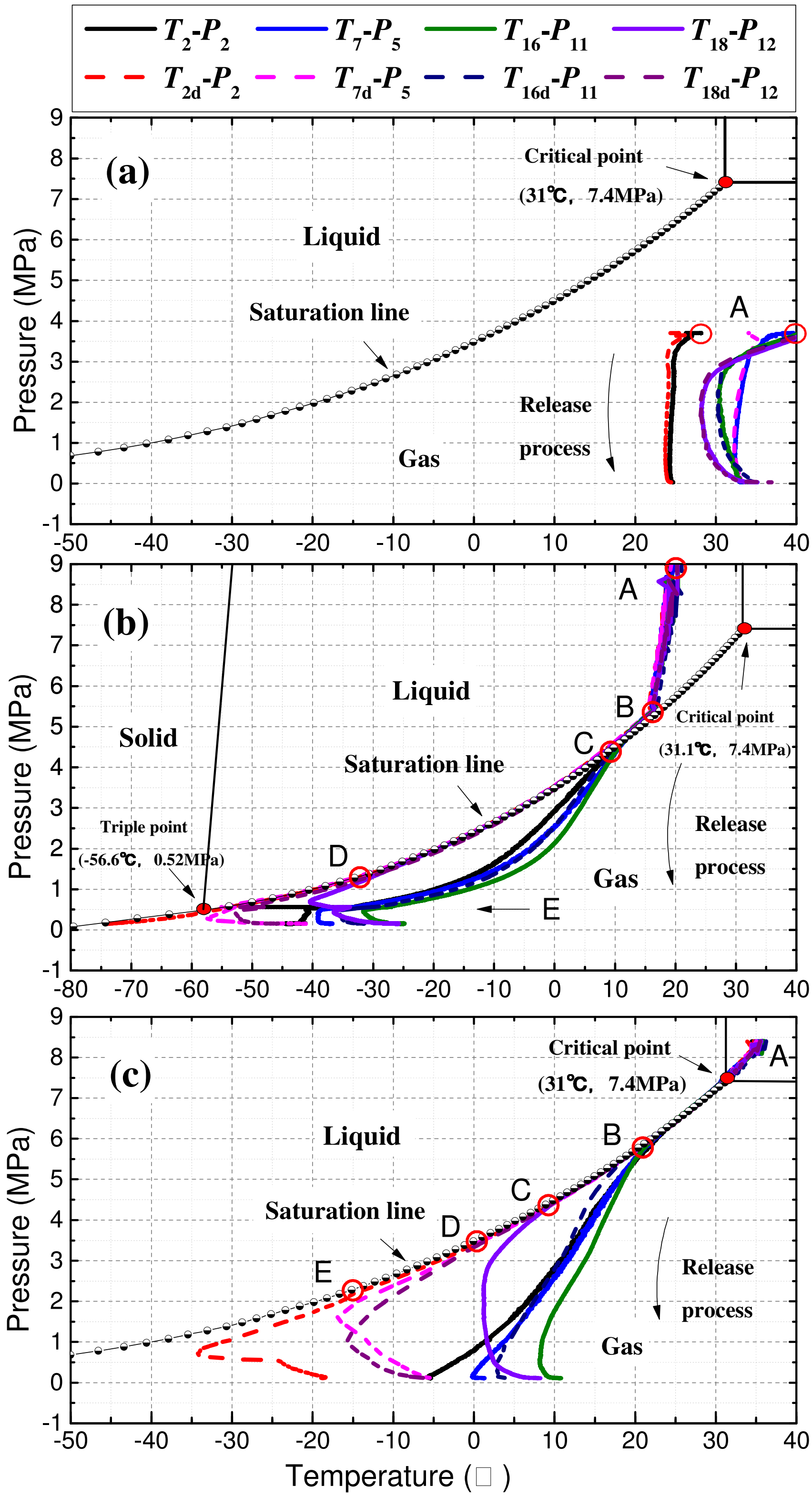

Fig. 8 Pressure-temperature developments with three CO_2 release experiments.

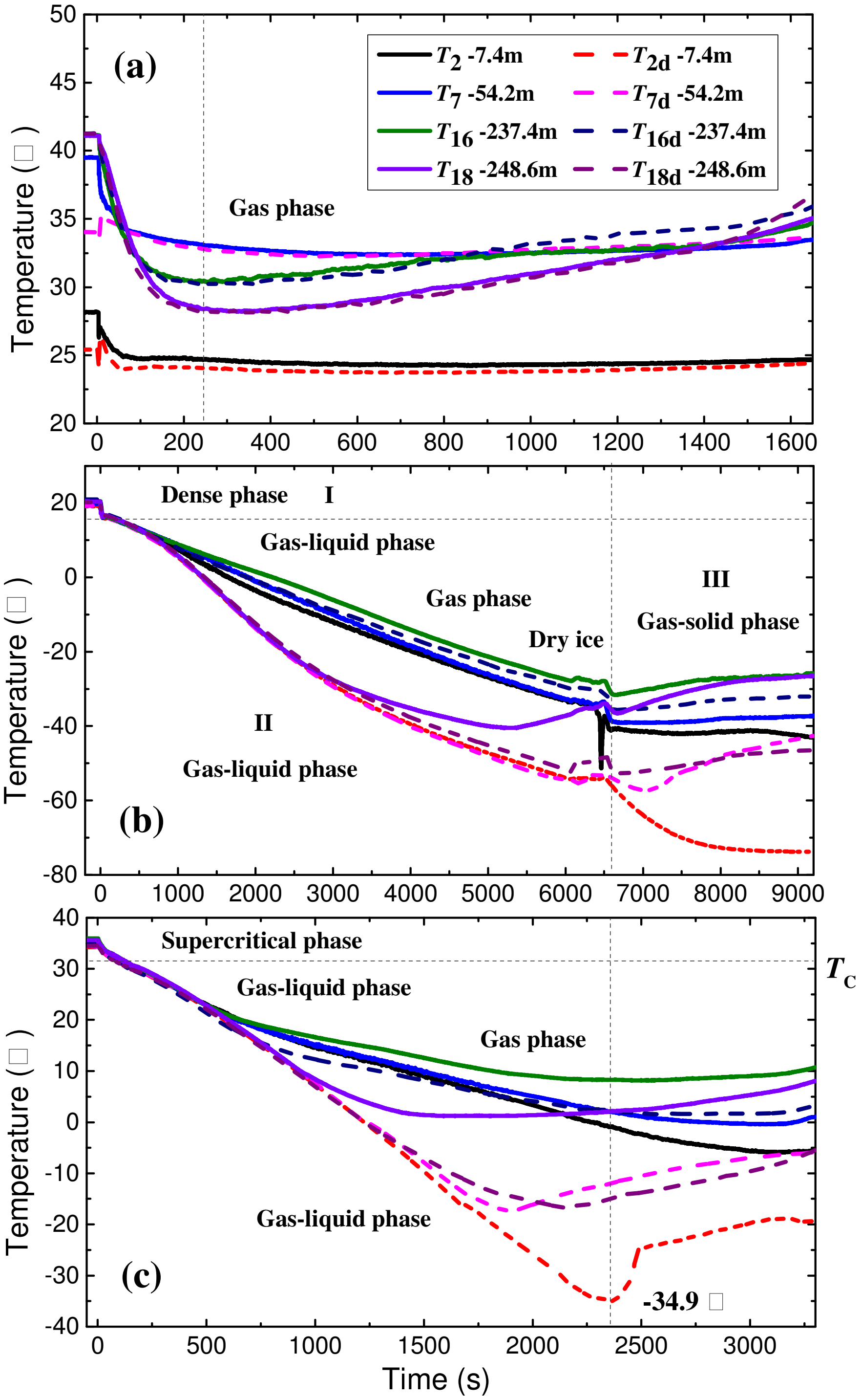

Fig. 9 Temperature evolutions with three CO_2 release experiments.

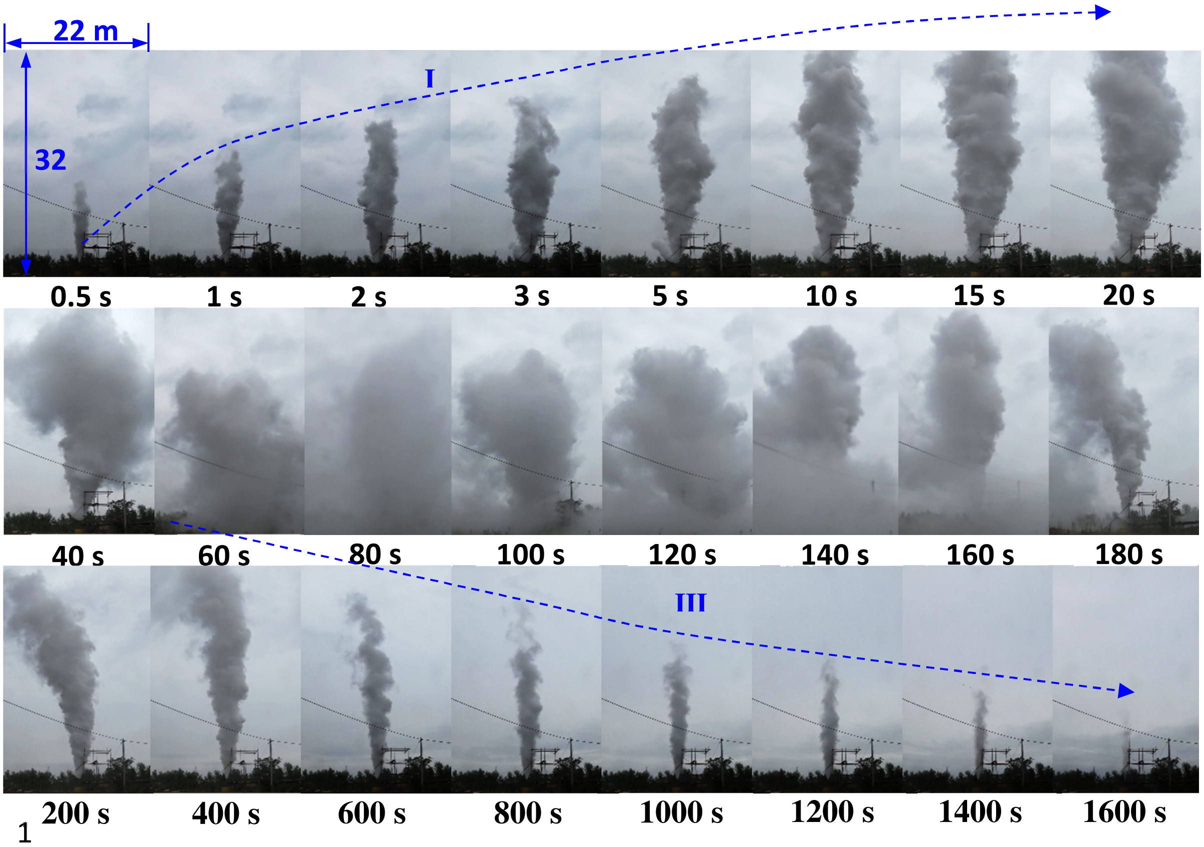

Fig. 10 Visible cloud development of the dense CO_2 release experiments.

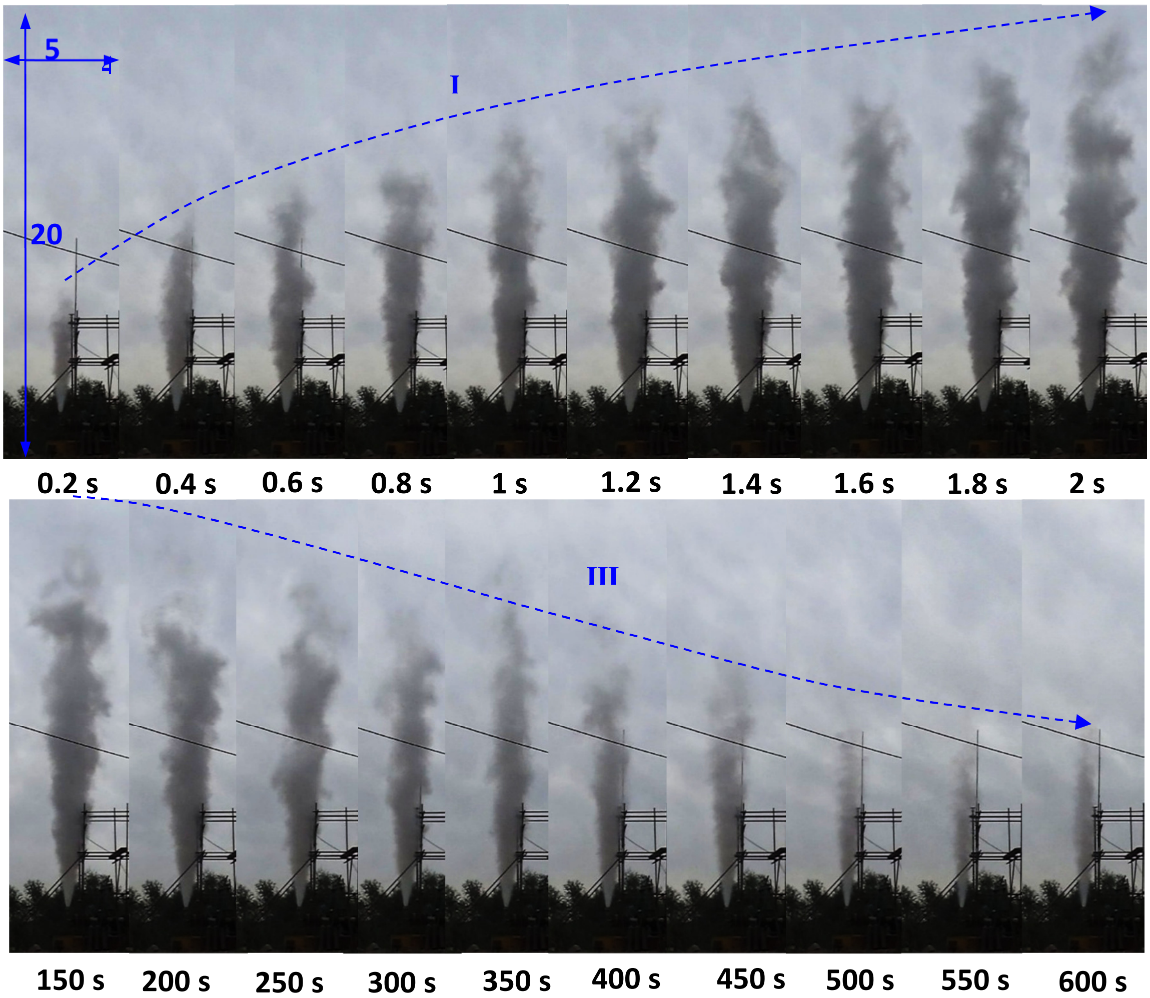

Fig. 11 Visible cloud development of the supercritical CO_2 release experiments.

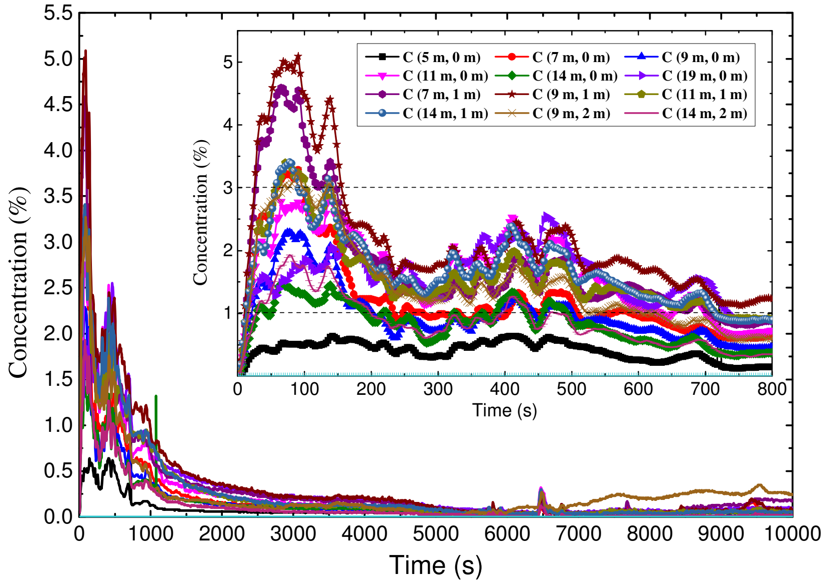

Fig. 12 CO_2 concentration distribution area of the dense CO_2 release experiments.

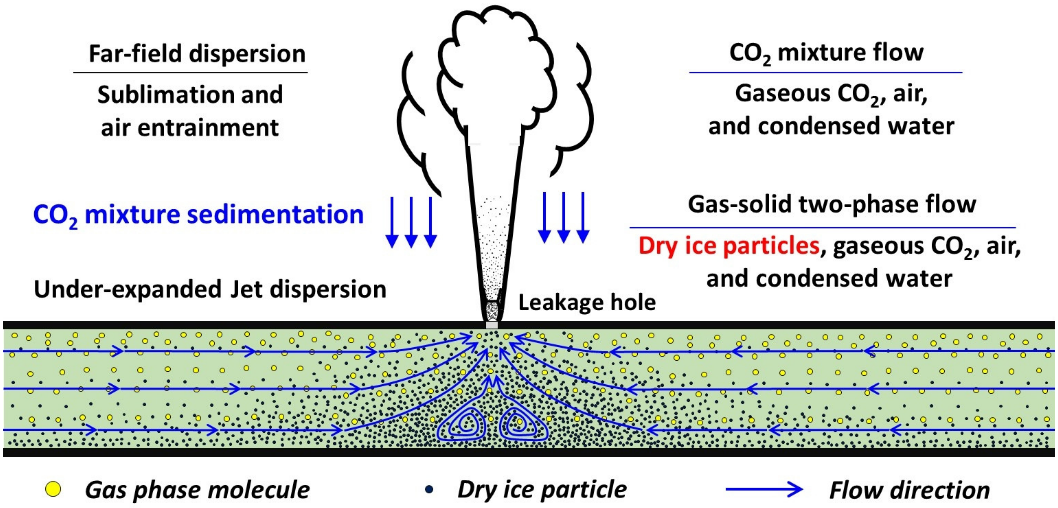

Fig. 13 Schematic of leakage process of high pressure CO_2.